Peer reviewed:

Yes, Chemical Engineering Science, 202 (2019) 194–207.

Title:

Dynamic pore-network modeling of air-water flow through thin porous layers

Author:

Chao-Zhong Qin[1], Bo Guo[2], Michael Celia[3], Rui Wu[4]

1. Department of Mechanical Engineering, Eindhoven University of Technology, the Netherlands
2. Department of Hydrology and Atmospheric Sciences, University of Arizona, United States
3. Department of Civil and Environmental Engineering, Princeton University, United States
4. Department of Mechanical Engineering, ShangHai JiaoTong University, China

Publication date:

1-2019

Copyright information:

Chemical Engineering Science 202 (2019) 194–207

Contents lists available at ScienceDirect

Chemical Engineering Science

journal homepage: www.elsevier.com/locate/ces

Dynamic pore-network modeling of air-water flow through thin porous layers

Chao-Zhong Qin [a,*], Bo Guo [b], Michael Celia [c], Rui Wu [d]

[a] Department of Mechanical Engineering, Eindhoven University of Technology, the Netherlands
[b] Department of Hydrology and Atmospheric Sciences, University of Arizona, United States
[c] Department of Civil and Environmental Engineering, Princeton University, United States
[d] Department of Mechanical Engineering, ShangHai JiaoTong University, China

HIGHLIGHTS

- Air-water flow through thin porous layers is studied using a state-of-the-art dynamic pore-network model.
- Our pore-scale results provide insight into the continuum-scale modeling of thin porous layers.
- We demonstrate the role of phase change in water removal from the cathode gas diffusion layer of a polymer electrolyte fuel cell.

GRAPHICAL ABSTRACT

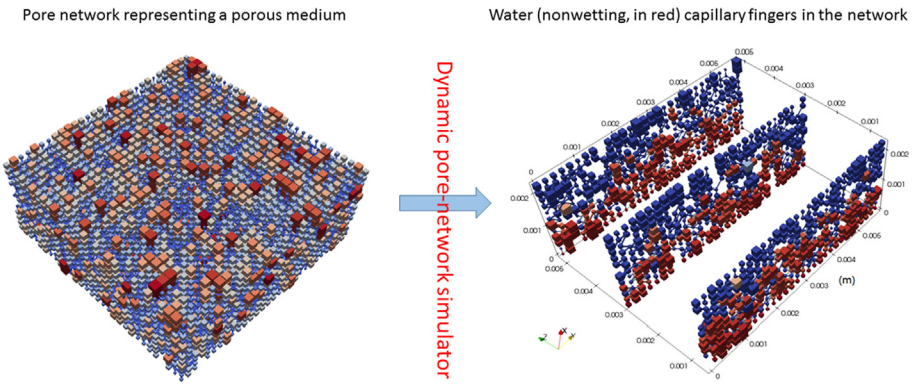

ARTICLE INFO

Article history:
Received 9 August 2018
Received in revised form 11 March 2019
Accepted 16 March 2019
Available online 16 March 2019

Keywords:
Thin porous media
Pore-network modeling
Two-phase flow
polymer electrolyte fuel cell (PEFC)
Water and heat management
Phase change

ABSTRACT

Thin porous layers, that have large aspect ratios, are seen in many applications such as hydrogen fuel cells and hygiene products, in which air-water immiscible flow is of great interest. Direct numerical simulations based on Navier-Stokes equation are computationally expensive, and even prohibitive for low capillary number flow such as water flooding in low-temperature polymer electrolyte fuel cells. Alternatively, the pore-network modeling needs much less computational resources, while still retaining essentials of the pore-structure information. In this work, a dynamic pore-network model of air-water flow with phase change has been developed. We focus on drainage processes through thin porous layers, in which liquid water is the nonwetting phase. Three test cases are conducted, namely, air-water flow through a thin porous layer, air-water flow through a bilayer of fine and coarse thin porous layers, and water flooding in the gas diffusion layer of a polymer electrolyte fuel cell with phase change between water and its vapor. Using these test cases, we aim to demonstrate the application of dynamic pore-network modeling in thin porous media studies. In particular, we discuss the challenge of modeling thin porous media at the average scale, and highlight the role of phase change in removing liquid water from the cathode gas diffusion layer.

* Corresponding author at: Department of Mechanical Engineering (office GEM-Z 3.135), Eindhoven University of Technology, PO Box 513, 5600 MB Eindhoven, the Netherlands.
E-mail address: chaozhong.qin@gmail.com (C.-Z. Qin).

https://doi.org/10.1016/j.ces.2019.03.038
0009-2509/

1. Introduction

Thin porous media are seen in a variety of applications, such as fuel cells, inkjets, filters, textiles, and hygiene products. In general, a thin porous medium/layer is characterized by its much larger lateral dimensions than the layer thickness, i.e., large aspect ratio (Prat and Agaësse, 2015; Qin and Hassanizadeh, 2014). Regulating flow and transport in thin porous layers plays an important role in the performance of their applications (Tavangarrad et al., 2018). For example, in a low-temperature polymer electrolyte fuel cell (PEFC), balancing hydration of electrolyte and liquid water flooding in thin diffusion layers is crucial to the cell performance and longevity, which is referred to as water management (Park et al., 2015).

At the continuum scale, the extended Darcy's law has been widely used to predict two-phase flow in porous media (Pinder and Gray, 2008). However, new challenges arise in modeling flow and transport through thin porous layers. They include heavy computational costs because of the meshing along layer thickness, failure of the REV (representative elementary volume) concept along layer thickness, and layer-layer interfacial effect (Qin and Hassanizadeh, 2015; Wargo et al., 2013). Over the past two decades, air-water flow through/in thin porous layers has gained much attention due to its important role in the operation of PEFCs. However, to date, it is still an open question if the framework of multiphase flow models, originally developed in hydrogeology and petroleum engineering, is suitable to the modeling of liquid water flooding in thin diffusion layers. In particular, the capillary number of water flow in an operating PEFC is extremely small, on the order of 10^{-8}. Such low-capillary flow may be beyond the applicability of the extended Darcy's law.

To gain insight into developing an efficient and reliable continuum-scale model of thin porous media, researchers resort to the pore-scale modeling (Médici and Allen, 2013; Qin, 2015; Sinha et al., 2007; Straubhaar et al., 2016; Wu et al., 2012a). Furthermore, the pore-scale modeling has been widely used to obtain material properties of porous media, such as capillary pressure, relative permeability, and effective diffusivity and thermal conductivity (García-Salaberri et al., 2015; Gostick et al., 2007; Wu et al., 2012b). Regarding two-phase flow in porous media, there are several pore-scale modeling approaches available, including direct numerical simulations (e.g., volume of fluid model (Qin et al., 2012c; Raeini et al., 2014), level-set model (Wang et al., 2009), lattice-Boltzmann model (Mukherjee et al., 2009), smoothed particle hydrodynamics (Kunz et al., 2016), Navier-Stokes-Cahn-Hilliard model (Shokrpour Roudbari et al., 2016)), and pore-network models (Huang et al., 2016; Joekar-Niasar et al., 2010; Sweijen et al., 2016; Thompson, 2002). In principle, direct numerical simulations can furthest preserve pore structures of porous media, which may be obtained by noninvasive visualization techniques. Significant computational resources, however, are required for direct simulations of two-phase flow in porous media, which makes the modeling of a REV-size porous medium prohibitive. This would be even worse when low capillary number flow is of interest. Alternatively, the pore-network modeling has attracted much attention because of much more computationally efficient. The basic idea of a pore-network model is as follows. First, the porous medium of interest is geometrically represented by a network of pore elements, in which pore bodies are used to denote large pore spaces while narrow regions between large pore spaces are denoted by pore throats. Then, flow and transport equations assisted by local rules are solved based on those pore elements, which are mostly idealized in shape. In the present work, we use a dynamic pore-network model to understand fundamentals of air-water flow through thin porous layers under low capillary number values. Water management in PEFCs is one of the typical relevant applications. In the following, water management in low-temperature polymer electrolyte fuel cells is introduced in Section 1.1. Then, a brief review of the pore-network modeling of two-phase flow in porous media is given in Section 1.2. Finally, we present the objectives of this work in Section 1.3.

1.1. Water management in low-temperature polymer electrolyte fuel cells

To provide sufficient power, a PEFC stack as shown in Fig. 1a is composed of hundreds of repeating units which are connected in series. A typical PEFC unit (see Fig. 1b) can be divided into the anode and cathode sides, with a solid electrolyte membrane sandwiched in between. Each side consists of a bipolar plate (BP) with grooved gas channels (GCs), a gas diffusion layer (GDL) coated with a micro porous layer (MPL), and a catalyst layer (CL). Its operating principles are as follows. Hydrogen and air are delivered into the GCs at the anode and cathode, respectively. At the anode, hydrogen diffuses through the GDL and evenly enters into the CL, where each hydrogen molecule splits into two electrons and two protons. Protons migrate into the cathode CL via the membrane, while electrons travel through an external circuit to the cathode side. At the cathode, electrons further transport into the CL through the solid phase, and oxygen diffuses into the CL, where they combine with protons and electrons to form water and heat. In automotive applications, the GDL, MPL, and CL usually have the thicknesses of $150 \sim 300$ μm, $20 \sim 50$ μm, and $5 \sim 30$ μm, respectively. In the in-plane, they can have the dimensions of around 50 cm by 50 cm. Thus, they are typically thin porous layers stacked upon each other.

A low-temperature PEFC has major advantages of quick startup and high efficiency. Usually, it operates below 90 °C. As a result, water management could be crucial, especially at high current densities. On the one hand, the electrolyte needs to attain high water content for effective proton conductivity; on the other hand, too much water would flood the diffusion layers and GCs, giving rise to the potential loss of mass transport. Therefore, in practice, both air and hydrogen are humidified before being delivered into the GCs, particularly to prevent electrolyte dehydration at the inlet region. What is more, water flooding is mitigated by increasing the stoichiometry at the cathode and proper designs of the GDL, MPL, CL, and GC. For instance, the diffusion layers are made hydrophobic for good water removal; and it has been shown that the MPL plays an important role in the mitigation of water flooding (Deevanhxay et al., 2013).

1.2. Pore-network modeling of two-phase flow in porous media

There has been a long history of the application of the pore-network modeling in two-phase flow studies of porous media. Quasi-static pore-network models are invasion-percolation based, which are widely used to obtain material properties of a porous medium (Blunt et al., 2002; Patzek, 2001). In comparison, a dynamic pore-network model is more complex and computationally expensive. Usually, thermodynamic variables are defined over each pore element, such as saturation and pressure. Mass conservation is solved for each pore body. In general, there are single-pressure and two-pressure pore-network models. A single-pressure model considerably reduces computational efforts. But, no local capillary pressure is defined in a pore body; a pore throat is assumed to be fully occupied by one phase; and, corner flow is neglected. As a result, some pore-scale dynamic events cannot be modeled. For example, Sinha and Wang (2007) used a single-pressure model to study liquid water transport in the GDL of a PEFC, in which spherical pore bodies and cylindrical pore throats were used.

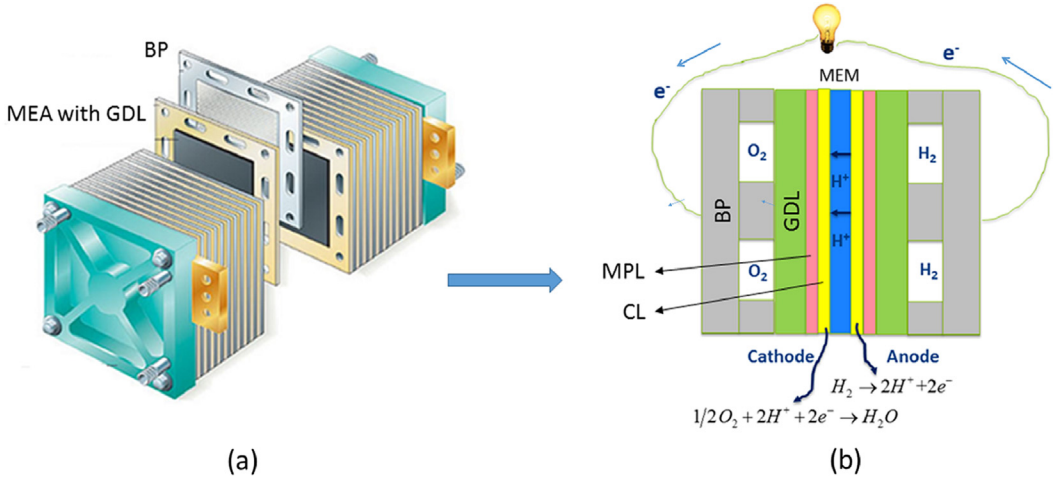

Fig. 1. (a) Schematic of a polymer electrolyte fuel cell (PEFC) stack; and (b) two-dimensional schematic of a PEFC unit.

In a two-pressure pore-network model, mass conservation equations of both phases are solved. In each pore body, two phase pressures are coupled by a local capillary pressure, which is geometrically determined by either wetting or nonwetting saturation. This corresponds to the assumption of local equilibrium. Since local capillary pressure is tracked in each pore body, this gives the possibility of including the effect of pore-body irregularity on two-phase flow dynamics in porous media. Meanwhile, corner flow in a pore body or pore throat can be easily implemented. In the literature, among many references, Thompson (2002) developed a dynamic two-pressure model to simulate fluid transport in disordered fibrous materials, Lee et al. (2009) developed a similar model to study liquid water transport in a hydrophobic GDL, and Joekar-Niasar et al. (2010) improved the dynamic pore-network modeling by introducing a semi-implicit scheme for the saturation equation. It was reported that this latter model provided more numerical stability, compared to previous models, particularly for unfavorable viscosity ratios and small capillary number values. Later on, Qin (2015) extended the model of Joekar-Niasar et al. into the study of water flooding in PEFCs. Also, evaporation was coupled with liquid water dynamics.

Dynamic pore-network models have been mostly used to qualitatively investigate fundamentals of two-phase flow in porous media (Joekar-Niasar et al., 2010; Lee et al., 2009; Qin, 2015). Few verification studies of the dynamic pore-network modeling exist in the literature, because (1) experimental data with high temporal resolution is difficult to obtain, and (2) highly simplified pore elements cannot well represent the complex pore structure. Recently, a comparison of the dynamic pore-network modeling of primary drainage against micromodel experiments has been reported (Yang et al., 2017). The authors showed that at the breakthrough, the distribution of the nonwetting phase saturation along the flow direction matches experimental data well. Also, there are a few verification studies of the quasi-static pore-network modeling, in which good matches of relative permeability and capillary pressure have been reported (Patzek, 2001; Valvatne and Blunt, 2004).

1.3. Objectives of this work

In this work, we extend our previous dynamic pore-network model with respect to the coupling algorithm between vapor transport and air-water two-phase flow, and use it to study air-water flow through thin porous layers under low capillary number values ($10^{-5} \sim 10^{-8}$). Because we focus on a qualitative understanding of the flow dynamics, we use artificial pore networks generated numerically by calibrating porosity and permeability. Liquid water is treated as the nonwetting phase. Through a number of case studies, we (1) explain why the extended Darcy's law cannot describe extremely low capillary number flow; (2) present two water drainage scenarios through a thin porous bilayer with the contrast of pore size (i.e. from fine to coarse and from coarse to fine layers); and (3) highlight the important role of phase change in determining liquid water flooding in the cathode GDL of a PEFC.

The paper is organized as follows. In Section 2, we briefly review our dynamic pore-network model with a focus on the discussion of coupling water vapor transport and air-water two-phase flow. The model is tested in terms of capillary pressure, and drainage rates under different viscosity ratios in Section 3. In Section 4, we present three case studies including air-water flow through a thin porous layer, air-water flow through a thin porous bilayer, and water flooding in the GDL of a PEFC. Implications from the case studies are discussed in Section 5, which is followed by conclusions given in Section 6.

2. Dynamic pore-network model

We present our dynamic pore-network model in three parts. The governing equations are presented in Section 2.1, which are complemented by the closure equations given in Section 2.2. In Section 2.3, the numerical implementation is described.

The following main assumptions are used in the dynamic pore-network model.

- Pore spaces are represented by idealized pore bodies. No volume is affiliated with pore throats (refer to Fig. 2 for the watershed concept used in the network extraction).
- Pore-space hydraulic and diffusive conductance is assigned to pore throats, which connect pore bodies together.
- Wetting phase is connected throughout the network via the corners of pore bodies and pore throats.
- Air and water are incompressible and immiscible.
- The dependence of air density and viscosity on water vapor concentration is neglected.

2.1. Governing equations

The volume conservation of each phase in a pore body is given as:

$$V_i \frac{ds_i^\alpha}{dt} = -\sum_{j=1}^{N_i} Q_{ij}^\alpha + \frac{r_i^\alpha}{\rho_i^\alpha}, \alpha = n, \quad w \tag{1}$$

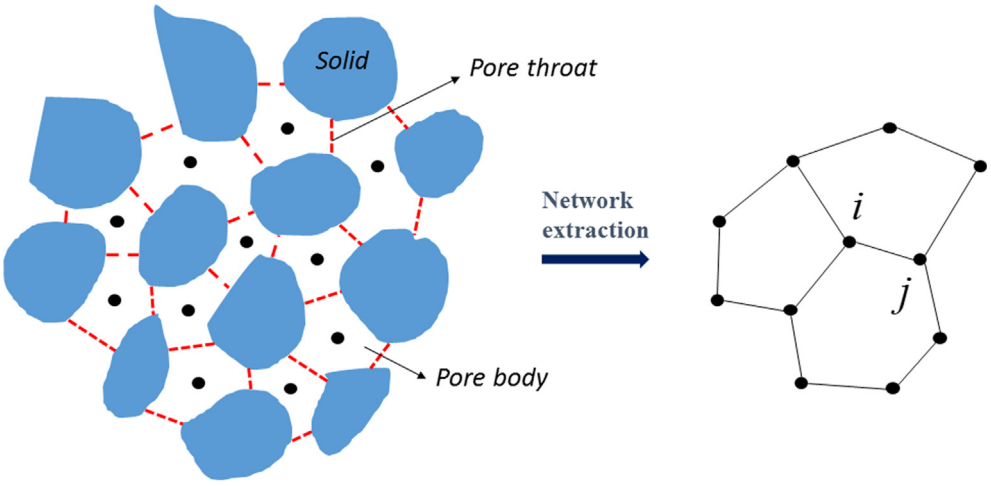

Fig. 2. Schematic of the representation of a porous medium by a pore network. In the left graph, the concept of watershed is used to generate discrete pore spaces, which are connected by pore throats. The right graph shows the extracted pore network composed of idealized pore bodies (i.e., nodes) and pore throats (i.e., bonds).

where i is the pore body index, ij is the pore throat index, a is the phase index with n and w denoting nonwetting and wetting phases, respectively, N_i is the coordination number of pore body i, V [m^3] is the volume, s [–] is the saturation, ρ [kg/m^3] is the density, Q_{ij} [m^3/s] is the flow rate from pore body i to pore body j, and r [kg/s] is the phase change term with the constraint of $r_i^w + r_i^n = 0$.

The flow rate of each phase through pore throat ij is calculated by Hagen-Poiseuille equation:

$$Q_{ij}^{\alpha} = K_{ij}^{\alpha}\left(p_i^{\alpha} - p_j^{\alpha}\right), \quad \alpha = n, \ \ w \tag{2}$$

where K_{ij}^{α} [m^3/Pa/s] is the α-phase conductance through the pore throat, p [Pa] is the pressure. Note that with Hagen-Poiseuille approximation, inertial effect cannot be considered which may be important along Haines jump fronts (Berg et al., 2013).

The capillary pressure in a pore body is related to the phase pressures by:

$$p_i^c = p_i^n - p_i^w \tag{3}$$

Casting Eqs. (1)–(3), together with the constraint of $s_i^w + s_i^n = 1$ and the definition of the mixture pressure of $\bar{p}_i = s_i^n p_i^n + s_i^w p_i^w$, we obtain the mixture pressure equation:

$$\begin{aligned}&\sum_{j=1}^{N_i}\left(K_{ij}^n + K_{ij}^w\right)\left(\bar{p}_i - \bar{p}_j\right)\\ &= -\sum_{j=1}^{N_i}\left\{\left[K_{ij}^n(1-s_i^n) - K_{ij}^w s_i^n\right]p_i^c + \left[K_{ij}^w s_j^n - K_{ij}^n\left(1-s_j^n\right)\right]p_j^c\right\}\\ &\quad +(1/\rho^n - 1/\rho^w)r_i^n\end{aligned} \tag{4}$$

Finally, in a pore body, the mass conservation of water vapor in the wetting phase (i.e., air) is given as (Qin, 2015):

$$\begin{aligned}\frac{d(C_i V_i^w)}{dt} &= -C_i\sum_{j=1}^{N_i}\max\left(Q_{ij}^w, 0\right) - \sum_{j=1}^{N_i} C_j \min\left(Q_{ij}^w, 0\right)\\ &\quad - \sum_{j=1}^{N_i} D_{ij}A_{ij}^w\frac{C_i - C_j}{L_{ij}} + r_i^w\end{aligned} \tag{5}$$

where C [kg/m^3] is the water vapor concentration, t [s] is the time, D_{ij} [m^2/s] is the diffusivity of water vapor, A_{ij}^w [m^2] is the wetting-phase flow area in the pore throat, and L_{ij} [m] is the pore throat length.

2.2. Closure equations

In this work, closure equations are given for an air-water system. To consider corner flow at the pore scale, pore bodies are assumed to be cubic, while pore throats are thin tubes with square cross-section. Inside a cubic pore body, the equilibrium relationship between capillary pressure and nonwetting saturation is semi-analytically given as (Joekar-Niasar et al., 2010; Qin, 2015):

$$p_i^c = \frac{2\sigma^{nw}\cos\theta}{R_i\left\{1 - \exp\left[-6.83\left(1 - s_i^n\right)\right]\right\}} \tag{6}$$

where σ^{nw} [N/m] is the air-water surface tension, R_i [m] is the radius of the inscribed sphere in the pore body, and θ [radian] is the static contact angle of air in porous media. A similar relationship was given in Lee et al. (2009).

The entry pressure of a pore throat is approximated by the Mayer and Stowe-Princen (MS-P) theory (Ma et al., 1996):

$$p_{ij}^e = \frac{\sigma^{nw}}{R_{ij}}\left(\cos\theta + \sqrt{\pi/4 - \theta + \sin\theta\cos\theta}\right) \tag{7}$$

where R_{ij} [m] is the radius of the inscribed circle in the cross-section of the pore throat. In a drainage process, a pore throat is invaded once the upstream capillary pressure exceeds its entry pressure.

Phase conductance is required in Eq. (2). If a pore throat is one-phase occupancy, the flow area of air phase is $A_{ij}^w = 4R_{ij}^2$. Then, based on the concept of hydraulic diameter, its conductance is approximated as:

$$K_{ij}^w = \frac{\left(A_{ij}^w\right)^2}{8\pi\mu^w L_{ij}} \tag{8}$$

where μ [Pa·s] is the dynamic viscosity. If a pore throat is two-phase occupancy, the flow areas of air and water are, respectively, given as (Ma et al., 1996):

$$A_{ij}^w = 4r_{ij}^2\left[\frac{\cos\theta}{\sin(\pi/4)}\cos\left(\frac{\pi}{4} + \theta\right) - \left(\frac{\pi}{4} - \theta\right)\right] \tag{9}$$

$$A_{ij}^n = 4R_{ij}^2 - A_{ij}^w \tag{10}$$

where r_{ij} is the radius of the curvature of air-water interface in the pore throat given by $r_{ij} = \sigma^{nw}\cos\theta/p_{ij}^c$. Then, the conductance of each phase is calculated as (Ransohoff and Engineering, 1988):

$$K_{ij}^{w} = \frac{A_{ij}^{w} r_{ij}^{2}}{\beta \mu^{w} L_{ij}}, \quad K_{ij}^{n} = \frac{\left(A_{ij}^{n}\right)^{2}}{8\pi \mu^{n} L_{ij}} \tag{11}$$

where β is a dimensionless resistance factor determined by the contact angle and the half corner angle of the cross section of a pore throat. Its full expression can be found in Qin et al. (2012a). We note that explicit expressions of the above constitutive relations are geometrically determined by idealized pore elements. For instance, Fig. 3 shows five different cross-sections of a pore throat, with different saturation values of inscribed circles for the nonwetting phase. If pore elements with complex shapes need to be considered for a realistic porous medium, the associated constitutive relations such as capillary-pressure-saturation relation in a pore body may be obtained using image analysis and direct numerical simulations (Riasi et al., 2016).

In the test case 3 of water flooding in the GDL (Section 4.3), phase change between liquid water and water vapor is involved. The following phase change model is used:

$$r_{i}^{n} = -k a_{i}^{nw} \left(C_{i}^{sat} - C_{i}\right) \tag{12}$$

where k [m/s] is the phase change rate constant, a_{i}^{nw} [m^2] is the interfacial area between nonwetting and wetting phases in the pore body (Joekar-Niasar et al., 2010), and C_{i}^{sat} [kg/m^3] is the saturated vapor concentration. The nucleation process of vapor condensation in dry pores is not considered. Therefore, in a pore body, the interfacial area is assumed to be equal to the wall area if the nonwetting saturation is smaller than 0.52 (the saturation value of inscribed sphere in the pore body).

Finally, the diffusivity of water vapor is empirically calculated by (Qin et al., 2012b):

$$D_{ij} = 0.2982 \times 10^{-4} \left(\frac{T}{333}\right)^{1.75} \left(\frac{101325}{p^{w}}\right) \tag{13}$$

where the temperature, T [K], and air pressure, p^w, in the pore throat are approximated by the values in its upstream pore body.

2.3. Numerical implementation

Governing Eqs. (1), (4), and (5) are numerically solved for three primary variables, namely, water saturation, s_i^n, mixture pressure, $\bar{p}_i$, and water vapor concentration, C_i (when phase change is considered). At the end of each time step, the remaining quantities are updated based on the primary variables. The numerical discretization of governing equations was given in detail in Qin (2015). We note that the semi-implicit scheme for water saturation update stabilizes the modeling at extremely small capillary number values. But, it can cause a little mass imbalance in a pore body. In our previous study, it was shown that the drainage modeling in the GDL was very time-consuming with a small capillary number value (e.g., 10^{-8}). This is because the time for filling a pore body is much longer than the time step determined by the criterion of Eq. A16 in Qin (2015). To reduce computational efforts, for the test case 3, we decouple liquid water transport into two parts: local accumulation due to phase change, and migration under capillary action. The reduced equation of water conservation, $V_i ds_i^n/dt = r_i^n/\rho_i^n$, can be solved with a large time step. In the interval of a few large time steps, we solve the full form of Eq. (1) for redistributing liquid water in the GDL, while the used time step is determined by Eq. A16 in [8]. In this way, computational efforts are considerably reduced. Also, we have checked that this numerical treatment has indiscernible effect on water transport in the GDL.

3. Capillary pressure and drainage rates

Before we present the case studies of air-water flow through thin porous layers, in this section, we test our model with respect to capillary pressure and drainage rates under different viscosity ratios of the nonwetting phase to the wetting phase. A small network of $10 \times 10 \times 10$ is numerically generated. The details of the network structure and physical parameters are given in Table 1. The nonwetting reservoir pressure (at X = 0 m) was set to 10000 Pa. At the outlet, the mixture pressure was set to zero, the wetting phase saturation was set to one, and the gradient of capillary pressure was set to zero. The periodic boundary condition was imposed to the four side faces. The flow is along the through-plane direction (positive X axis).

Fig. 4a shows the comparisons among the quasi-static capillary pressure, the capillary pressure under dynamics, and the phase pressure difference (mass-averaged over the whole network) versus the wetting saturation over the whole network. It is seen that the capillary pressure curve under dynamics is above the quasi-static one, while the curve of the phase pressure difference is even higher than the capillary pressure curve under dynamics. The difference between the phase pressure difference and the capillary pressure is characterized by the well-known tau term as follows: $p^n - p^w - p^c = -\tau \partial S^w/\partial t$, where S^w is the network wetting saturation, and τ is a material property which needs to be experimentally determined (Hassanizadeh and Gray, 1990). The same observations have been found in both experiments (Zhuang et al., 2017) and direct numerical simulations (Kunz et al., 2016). Then, we reduced the viscosity of the wetting phase to test the dependence of the drainage rate on the viscosity ratio of the nonwetting phase to the wetting phase. Fig. 4b shows the drainage rates under three different viscosity ratios of 54 corresponding to an air-water system, 1.0, and 0.1 corresponding to an unfavorable drainage process. As expected, the drainage rate decreases notably as the viscosity ratio decreases. Meanwhile, the drainage front evolves to a viscous-finger pattern with the viscosity ratio of 0.1.

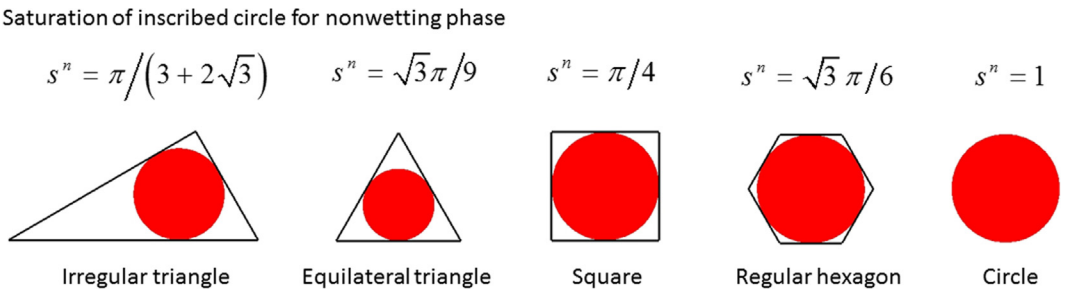

Fig. 3. Schematic of the nonwetting phase (in red) occupancies in five different cross-sections of a pore throat. The saturation value of each inscribed circle for the nonwetting phase is also given. (For interpretation of the references to colour in this figure legend, the reader is referred to the web version of this article.)

Table 1
Pore-network structure and physical properties[a] used in model test.

Lattice distance	2.0×10^{-4} m
Domain size, x × y × z (in lattice)	12 × 10 × 10
Number of pore bodies and pore throats	1163/2552
Minimum/maximum/mean size of pore body[b]	2.0×10^{-5} m/1.0×10^{-4} m/5.0×10^{-5} m
Standard deviation of truncated lognormal distribution	0.4
Porosity	0.22
Permeability	7.7×10^{-12} m^2
Air-water surface tension	0.0728 N/m
Contact angle for water	0 rad
Water/air viscosity	1.0×10^{-3}/1.84×10^{-5} Pa·s
Water/air density	998/1.204 kg/m^3

[a] Properties are given at the room temperature (20 °C).
[b] The size of a pore body means the radius of the inscribed sphere in the pore body.

Table 2
Pore-network structure used in test case 1, and physical properties[a] used in test case 1 and 2.

Lattice distance	2.0×10^{-4} m
Domain size, x × y × z (in lattice)	12 × 10 × 10
Number of pore bodies and pore throats	10619/23781
Minimum/maximum/mean size of pore body[b]	2.0×10^{-5} m/1.0×10^{-4} m/5.0×10^{-5} m
Standard deviation of truncated lognormal distribution	0.4
Porosity	0.2
Permeability	7.5×10^{-12} m^2
Air-water surface tension	0.0728 N/m
Contact angle for water	0 rad
Water/air viscosity	1.0×10^{-3}/1.84×10^{-5} Pa·s
Water/air density	998/1.204 kg/m^3

[a] Properties are given at the room temperature (20 °C).
[b] The size of a pore body means the radius of the inscribed sphere in the pore body.

4. Modeling of air-water flow through thin porous layers

To pursue the objectives given in Section 1.3, three test cases have been run. They include (1) air-water flow through a thin porous layer, (2) air-water flow through a bilayer of fine and coarse thin porous layers, and (3) water flooding in the GDL of a PEFC with phase change between liquid water and water vapor. In the following, numerical setups and results of the case studies are presented in detail.

4.1. Air-water flow through a thin porous layer

In this test case, we mainly present water distribution profiles through a single thin layer under different operation conditions. Later on, in Section 5, we will discuss its continuum-scale modeling.

Here, an artificial thin porous layer was created. The network information is given in Table 2. Along the through-plane direction, there are 10 layers of pores excluding inlet and outlet pores, which gives a layer thickness of 2.0 mm. Fig. 5 shows the detailed pore-network information including the pore-body size and coordination number distributions, which are similar to those used in the model test in Section 3. The size of a pore throat was correlated with the sizes of its two connected pore bodies (Joekar-Niasar et al., 2010). Two types of inlet boundary condition were tested (at X = 0 m), namely, uniform pressure boundary condition and uniform flux boundary condition (Fazeli et al., 2015). The remaining numerical settings are the same as given in Section 3 for the model test.

Fig. 6 shows the water pressure and capillary pressure distributions along the through-plane direction when a nearly steady-state situation was reached (Qin, 2015). Based on the curve of quasi-static capillary pressure versus saturation in Fig. 4a, three inlet water pressure values were used, namely, 4000 Pa, 5000 Pa, and 7000 Pa. At 4000 Pa, the capillary front of water stopped in the middle of the layer without a breakthrough. As such, a uniform distribution of the water pressure is seen in Fig. 6. The water phase pressure is very close to the capillary pressure although they have different definitions at the average scale. Notice that at 5000 Pa, small fluctuations of pressure along the flow direction are due to the heterogeneity of pore sizes. They are expected to be smoothed out as increasing the network size.

Fig. 7 shows the temporal evolutions of network-averaged capillary pressure and phase pressure difference at the inlet water pressure of 7000 Pa. As more and more water invaded into the layer, the difference between capillary pressure and phase pressure difference decreased to the value of around 250 Pa. This difference is much smaller than the capillary pressure. Two temporal evolutions of capillary number values during the drainage process are given in Fig. 8. It is seen that even small inlet water pressure values gave rise to relatively large capillary number values. This is because of the low viscous resistance of a thin porous layer.

Fig. 9 shows the water saturation profiles along the through-plane direction. Clearly, saturation values increased as the increase

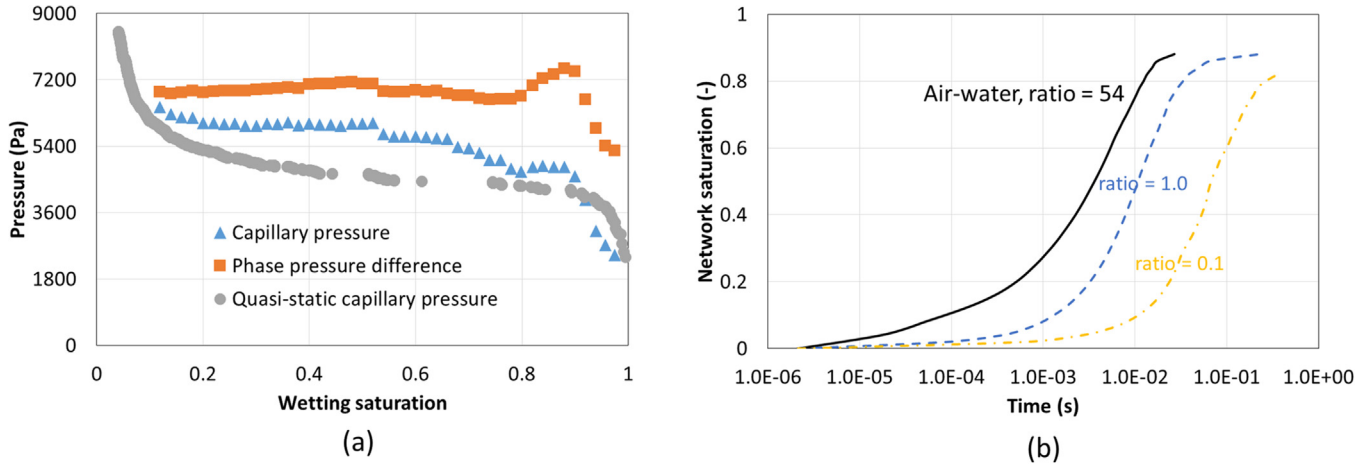

Fig. 4. (a) Distributions of the quasi-static capillary pressure, the capillary pressure under dynamics, and the phase pressure difference versus the network saturation; (b) the drainage rates under three different viscosity ratios of the nonwetting phase to the wetting phase: 54, 1.0, and 0.1.

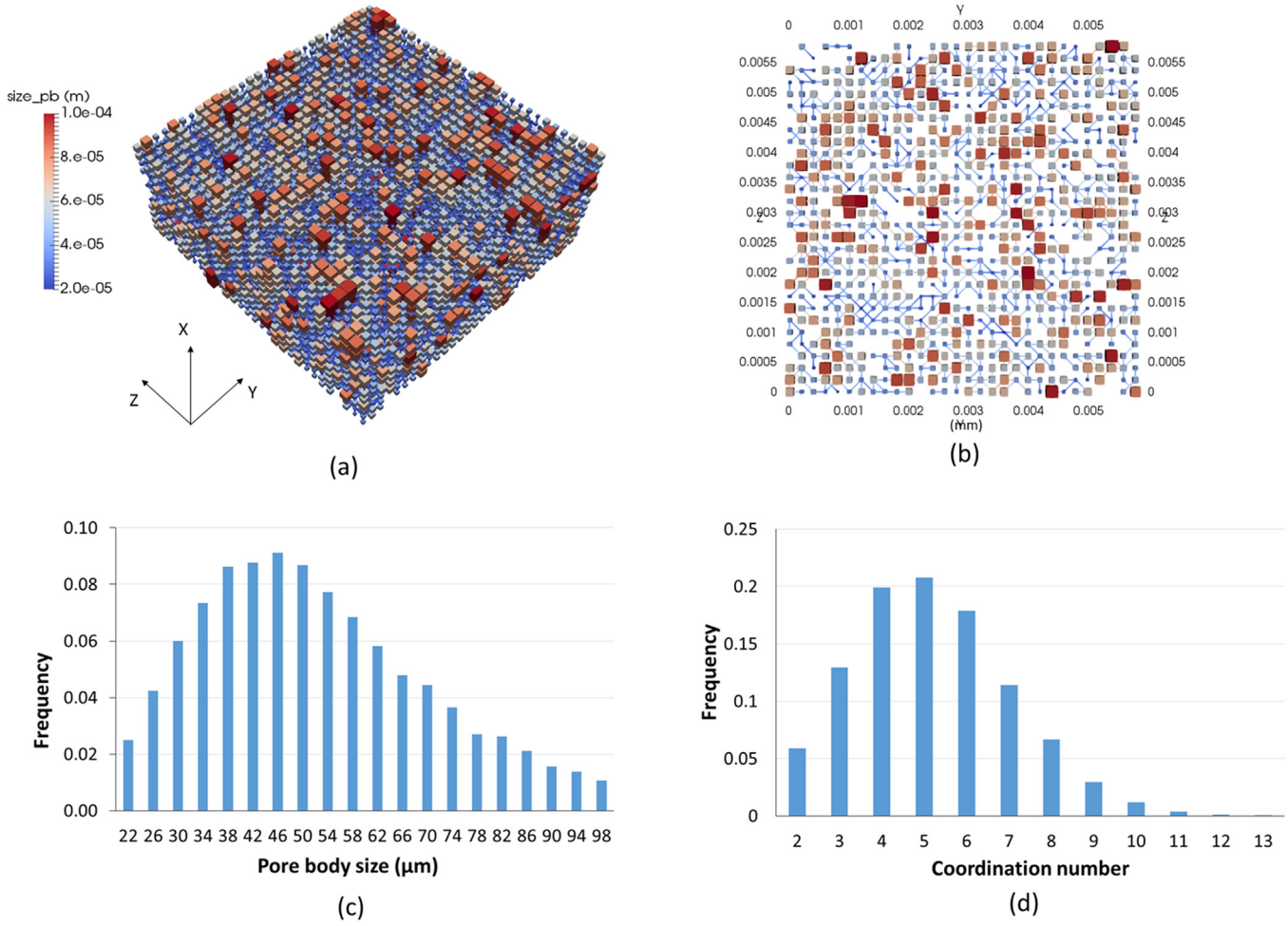

Fig. 5. Pore-network information used in the test case 1 of air-water flow through a thin porous layer: (a) 3D pore network colored by pore-body size; (b) connectivity of pores in a Y-Z plane; (c) pore-body size distribution; and (d) coordination number distribution.

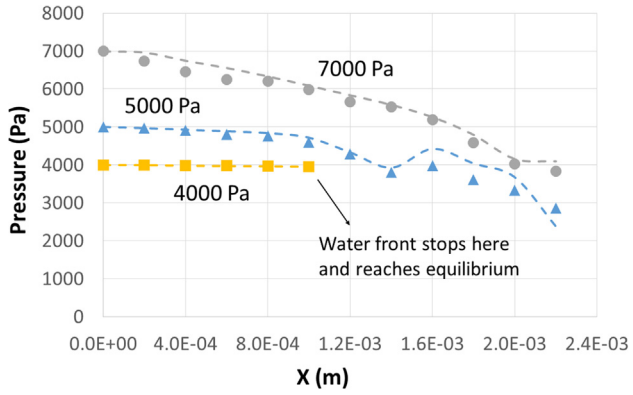

Fig. 6. Distributions of water pressure and capillary pressure along the through-plane direction. The pressure values are averaged over each cross section. The markers show capillary pressure values which are specific-area (between nonwetting and wetting) weighted. The dashed lines show water pressure values which are mass-weighted. Three inlet nonwetting-phase pressure values, namely, 4000 Pa, 5000 Pa, and 7000 Pa, were studies. No breakthrough of water was obtained for the inlet pressure value of 4000 Pa.

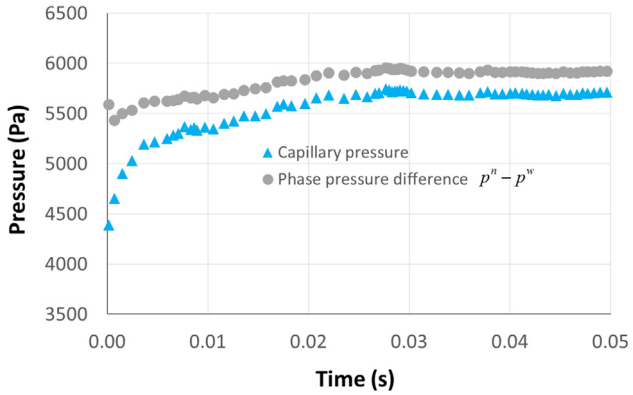

Fig. 7. Temporal evolutions of capillary pressure and phase pressure difference at the inlet water pressure of 7000 Pa. All pressure values are averaged over the entire network. The capillary pressure is interfacial-area-weighted, while the phase pressures are mass-weighted.

of the inlet water pressure. Meanwhile, there was an obvious switch of the shape of saturation profile, i.e., from concave to convex. However, at the continuum scale, for capillary dominant water flow, the Richards equation together with the widely used power-law relative permeability and Leverett J function of capillary pressure (Wang and Wang, 2008), predicts only a convex profile of water saturation distribution. This is because d^2s/dx^2 (s denotes the water saturation, and x is the spatial coordinate) is always negative for the entire range of saturation values. A concave shape of the saturation distribution may indicate that the flow and

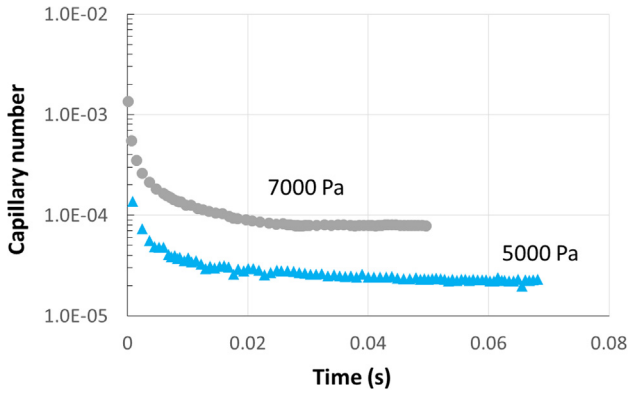

Fig. 8. Temporal evolutions of capillary number values during the drainage process. The capillary number is defined as $u_{in}\mu^n/\sigma^{nw}$, where u_{in} is the inlet flux of liquid water.

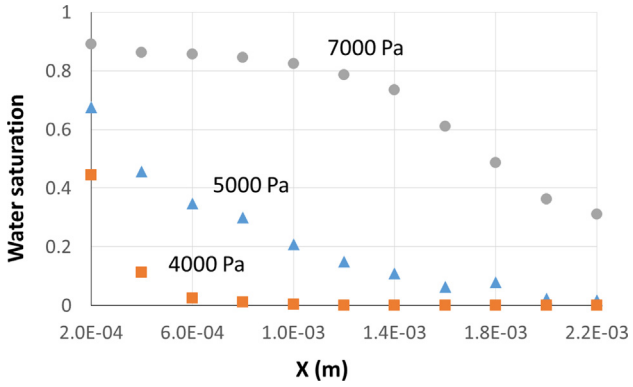

Fig. 9. Distributions of water saturation along the through-plane direction at three different inlet water pressure values, namely, 4000 Pa, 5000 Pa, and 7000 Pa.

transport is close to quasi-static, which corresponds to a very small capillary number value.

Under the uniform flux boundary condition, a flow rate of liquid water was introduced into the network by means of source term in the water conservation Eq. (1). This type of boundary condition is relevant to the water flooding in the GDL of a PEFC. Fig. 10 shows the water saturation distributions under four different capillary number values. A high current density of 1.5 A/cm^2 in the operation of a PEFC (Qin et al., 2012b) corresponds to a capillary number

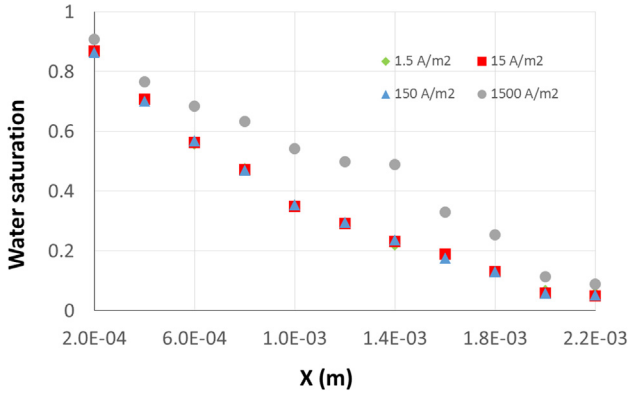

Fig. 10. Distributions of water saturation along the through-plane direction under uniform flux boundary condition. The current density of 1.5 A/cm^2 corresponds to a capillary number value of around 1.8×10^{-8}.

value of around 1.8×10^{-8}, which is extremely small. It is seen that increasing the capillary number value by 100 times had negligible influence on the water saturation distribution in the layer. Also, the profile of water saturation along the layer thickness showed a concave shape, which is in accordance with the experimental observation in Lee et al. (2015). For an assumed current density of 1500 A/cm^2 (corresponding to a capillary number value of 1.8×10^{-5}), more liquid water accumulated in the layer and the saturation profile started to switch to a convex shape.

From Figs. 9 and 10, we conclude that for a thin porous layer, the shape of cross-sectional saturation profile evolves from concave to convex with the increase of capillary number. Finally, Fig. 11 shows the snapshot of liquid water distribution in the network at the inlet water pressure value of 7000 Pa. Clearly, liquid water showed a capillary-type distribution pattern.

4.2. Air-water flow through a bilayer of fine and coarse thin porous layers

In practice, a number of thin porous layers, varying in material properties and pore structures, are stacked upon each other to regulate flow and transport processes. Diapers and PEFCs are two typical applications, in which unsaturated water flow is of great interest (Diersch et al., 2011; Lee et al., 2015; Morgan and Datta, 2014). In this test case, we have investigated drainage processes in a bilayer of fine and coarse thin porous layers (Belgacem et al., 2016; Ji et al., 2010). Still, liquid water is the nonwetting phase. To reduce the computational effort, in the Z direction, only one layer of pores was generated to represent the coarse porous layer. The parameters used for the network generation are the same as those in the test case 1 (see Table 2), except that the generated coarse layer has around 400 pore bodies and 865 pore throats. Then, reducing the mean pore size and the lattice distance by five times, the fine layer was generated with the domain size of $10 \times 196 \times 6$ lattices (lattice distance of 4.0×10^{-5} m) along the X, Y, and Z direction, respectively. Finally, the two layers were combined at the layer-layer interface by constructing interface pore throats. The detail can be found in Qin et al. (2016).

Two different drainage processes were investigated. One is that liquid water invaded into the domain from the fine layer, while the other is that liquid water invaded into the domain from the coarse layer. In either process, two pressure values (25000 Pa and 30000 Pa) of the water reservoir were employed, which are slightly larger than the breakthrough pressure value. The wettability of the bilayer was assumed to be uniform. The same physical and fluid properties as those in the test case 1 were used.

Fig. 12a shows the liquid water penetration patterns from the fine layer to the coarse layer. It is seen that the water distribution in the coarse layer was directly related to the breakthrough points at the layer interface. This is because the capillary barrier in the coarse layer is much smaller than that in the fine layer. Fig. 13a shows the water distributions along the through-plane direction after drainage processes. There was a huge jump of the saturation at the interface only under the high reservoir pressure of 30000 Pa. Under the low reservoir pressure of 25000 Pa, only three breakthrough points were observed at the interface. As a result, a non-monotonic water profile was built along the through-plane direction under the capillary action.

Fig. 12b shows the liquid water penetration patterns from the coarse layer to the fine layer. Due to the much higher capillary barrier of the fine layer, the coarse layer was almost saturated with liquid water before water could further penetrate the fine layer. The water content in the fine layer was directly related to the water reservoir pressure at the inlet. The corresponding water distributions along the through-plane direction are shown in Fig. 13b. It is seen that water was quite uniformly distributed in the coarse

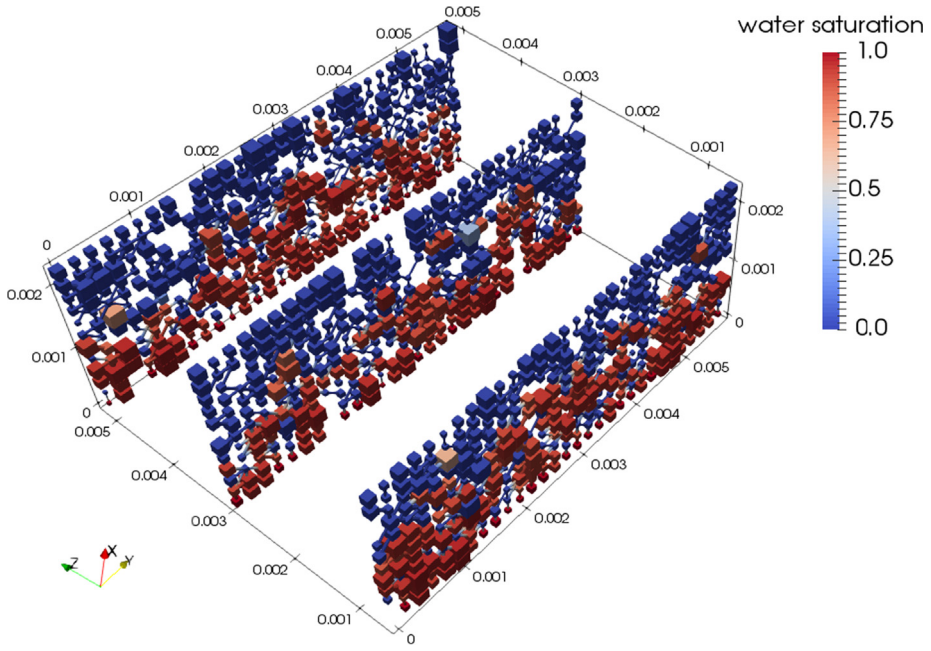

Fig. 11. Snapshot of liquid water distribution in the layer at the inlet water pressure value of 7000 Pa. The axis unit is meter.

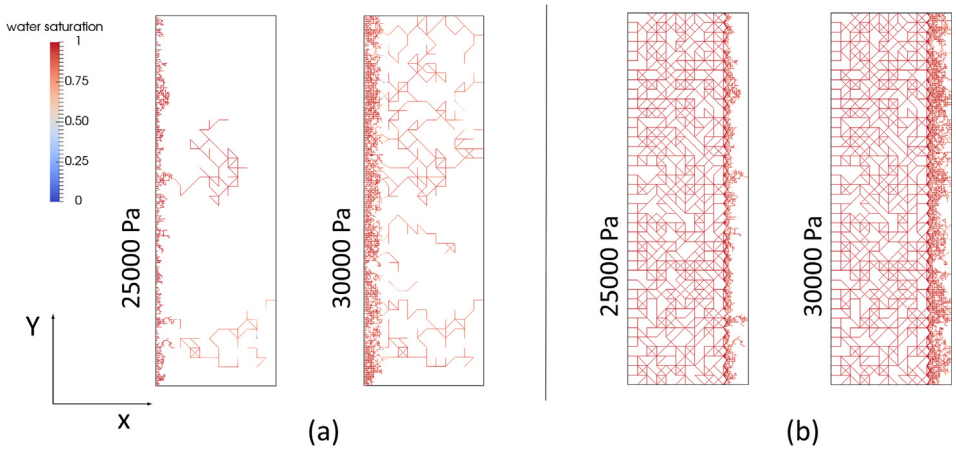

Fig. 12. Liquid water distributions in a bilayer after drainage processes under the constant pressure boundary condition: (a) liquid water invades the domain from the fine porous layer; and (b) liquid water invades the domain from the coarse layer. The invaded pores are denoted by the red. The empty is the uninvaded area.

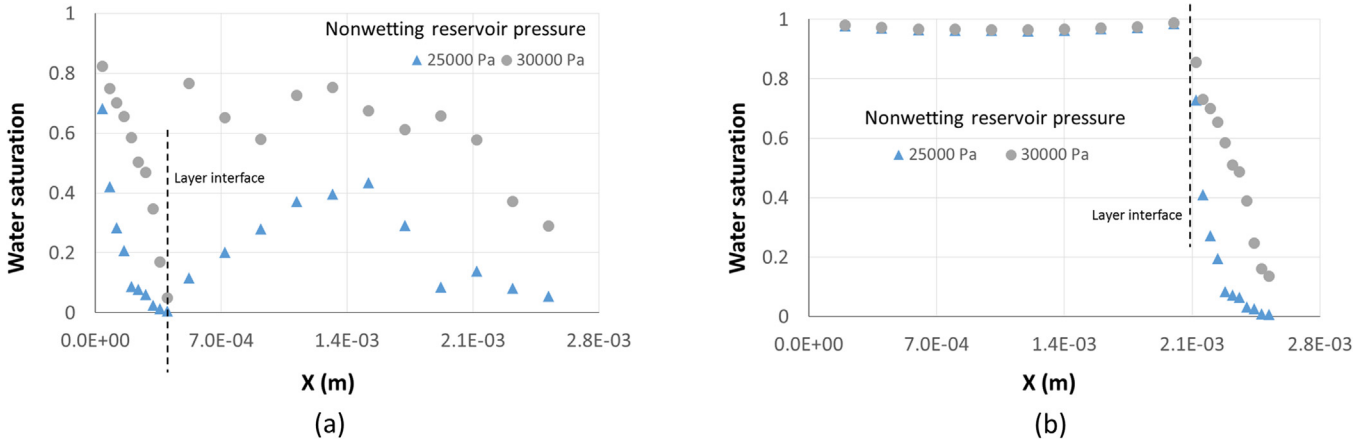

Fig. 13. Distributions of water saturation along the through-plane direction after drainage processes: (a) from the fine to the coarse; and (b) from the coarse to the fine. The dashed vertical line marks the interface location between the two layers.

layer. Furthermore, it is observed that the water profile was concave under the low reservoir pressure of 25000 Pa, while convex under the high reservoir pressure of 30000 Pa. In the PEFC operation, placing a fine layer above the GDL would cause the severe flooding of the GDL, which will shut down the cell immediately (Owejan et al., 2010).

4.3. Water flooding in the cathode GDL of a PEFC

It is well known that phase change between liquid water and water vapor plays an important role in the water management (Basu et al., 2009). A large temperature gradient along the GDL thickness can be built up by decreasing its thermal conductivity. This helps water removal mostly in the vapor form, which is similar to the heat pipe effect (Wang and Wang, 2008). In this test case study, we demonstrate, at the pore scale, two possible water flooding scenarios in the GDL. Given the fact that the in-plane thermal conductivity is much larger than the through-plane one (Sadeghifar et al., 2014), as a first attempt, a linear temperature distribution along the through plane of the GDL was assumed based on the cell voltage and current density, and the GDL thermal conductivity. The latent heat released by phase change was also lumped into the assumed temperature gradient.

The used pore network for an uncompressed GDL, fluid properties, and operating conditions are given in Table 3. A large value of the phase change coefficient was chosen to approximate the local equilibrium condition between water and its vapor. A typical cell operating temperature of 80 °C was used. The saturated vapor concentration, C_i^{sat}, is dependent on the temperature given in Qin et al. (2012b). Two thermal conductivity values of the GDL were used, namely, 0.6 W/m k and 0.3 W/m k (Owejan et al., 2010). Given a low thermal conductivity of the MPL, water would enter into the GDL in the vapor form. In the GDL, liquid water may form due to the phase change. The inlet vapor flux was calculated from the current density. At the outlet, water vapor was saturated under the channel area; and no flux boundary condition was imposed under the land area (see Fig. 14). The GC is assumed to be free of liquid water such that the same boundary condition for water phase as in the test case 1 was used here.

Table 3
Pore-network structure, fluid properties,[a] and operating conditions used in test case 3.

Lattice distance	2.5×10^{-5} m
Domain size, x × y × z (in lattice)	12 × 40 × 10
Number of pore bodies and pore throats	4686/10190
Minimum/maximum/mean size of pore body[b]	9.0×10^{-6}/1.1×10^{-5} m/1.25×10^{-5} m
Standard deviation of truncated lognormal distribution	0.1
Porosity	0.81
Though-plane permeability	3.5×10^{-12} m^2
Air-water surface tension	0.0625 N/m
Contact angle for water[c]	0 rad
Water/air viscosity	3.5×10^{-4}/2.12×10^{-5} Pa·s
Water/air density[d]	972/2.0 kg/m^3
GDL thermal conductivity, scenario 1/ scenario 2	0.6 W/m k/0.2 W/m k
Cell temperature	80 °C
Cell current density	1.0 A/cm^2
Cell voltage[e]	0.68 V
Relative humidity in the GC	100%
Phase change coefficient, k	1.0 m/s

[a] Fluid properties are given at the temperature of 80 °C.
[b] The size of a pore body means the radius of the inscribed sphere in the pore body.
[c] A fully hydrophobic GDL is assumed.
[d] The operating pressure is 2 bar.
[e] The cell voltage is assumed based on a typical polarization curve of a PEFC (Owejan et al., 2010).

Fig. 14 shows the temporal evolutions of liquid water clusters in the GDL. For the GDL with the high thermal conductivity (0.6 W/m k), the temperature difference through the GDL is around 1.8 °C. Liquid water emerged throughout the GDL, mostly under the land area. Later on, liquid water started to spread under the capillary action (the top row in Fig. 14). Fig. 15a shows the corresponding water distributions along the through-plane direction. It is seen that at the beginning (30 s) more water was observed at the outlet of the GDL. Afterwards, water preferentially accumulated at the inlet due to the blocking of pores. At the steady state, the distribution profile was nonmonotonic with the lowest water saturation close to the outlet region.

For the low thermal conductivity (0.3 W/m k), the GDL has high capacity of water removal in the vapor form. At the beginning, liquid water was only seen under the land area due to the mass transfer limitation (the bottom row in Fig. 14). Later on, water mitigated back to the GDL inlet mainly under the land area. Once large interfacial areas between liquid and gas phases were built up, the simulation reached the steady state. Around 60% of the inlet water was removed in the vapor form by molecular diffusion, while the rest was removed in the liquid form assisted by the phase change. What is more, the GDL under the channel area was dry. Fig. 15b shows the distributions of water saturation along the through-plane direction. High saturation was seen at the outlet, while low saturation at the MPL-GDL interface. Obviously, this type of saturation profile was caused by the phase change.

5. Discussion

The extended Darcy's law has been widely used in the modeling of two-phase flow through thin porous layers (Pinder and Gray, 2008). However, for a layer with only a few pores along the thickness (e.g. GDLs of a PEFC and top sheets of a diaper), the REV support fails. This causes the confusion and difficulty in explaining numerical results along the layer thickness from the extended Darcy's law. Second, the dimension of a layer-layer interface is usually comparable to layer thickness. This indicates the importance of layer-layer interfaces in flow and transport through stacked thin porous layers (Tavangarrad et al., 2018). However, how to incorporate this effect into some measurable material property used in the Darcy's law is still unclear. Recently, we reformulated flow and transport through thin porous layers with thickness-averaged material properties, which is called the reduced continua model (RCM) (Qin and Hassanizadeh, 2015, 2014; Tavangarrad et al., 2018). In the RCM, layer-scale material properties are experimentally measurable. Further, it reduces the 3D modeling to the 2D, which is much more computationally efficient. It is noted that through-plane distribution information is lost due to the averaging over the layer thickness.

Capillary pressure and relative permeability, as two key material properties, need to be provided in the extended Darcy's law. In convention, they are determined by experiments which were operated under pressure conditions (Zhuang et al., 2017). For instance, to obtain the capillary pressure saturation curve for the primary drainage, the sample under test is connected to a nonwetting reservoir on one side, and connected to a wetting reservoir on the other side. The curve is obtained by continuously increasing the nonwetting reservoir pressure with a small increment. However, in the test case 1, we showed that a very small capillary number value could not be reached under the pressure boundary condition (Fig. 8). This indicates that material properties obtained in the conventional way would not apply to the case of an extremely small capillary number flow, for instance, a capillary number value of 10^{-8} in the water flooding of a PEFC. We also showed that water distribution in the layer was insensitive to the imposed flow

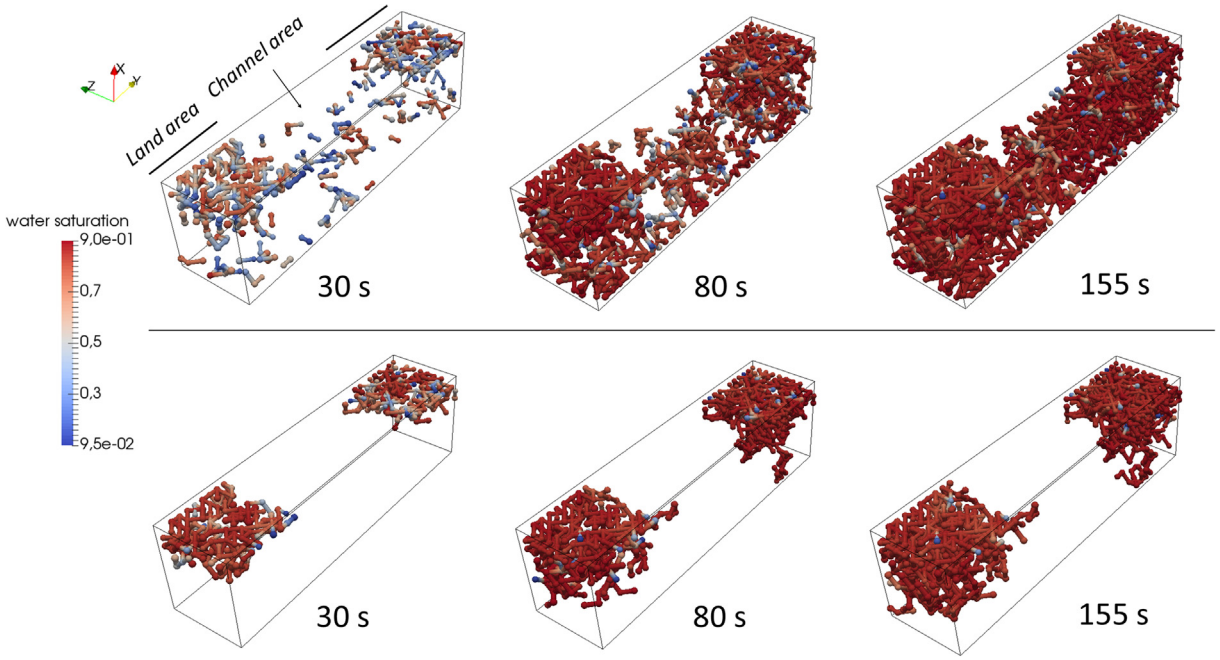

Fig. 14. Temporal liquid water distributions in the GDL. The top is the scenario 1 with the high thermal conductivity of 0.6 W/m k; and the bottom is the scenario 2 with the low thermal conductivity of 0.3 W/m k. For better visualization, invade pore bodies are represented by spheres, while invaded pore throats are represented by cylinders. The empty is the dry area.

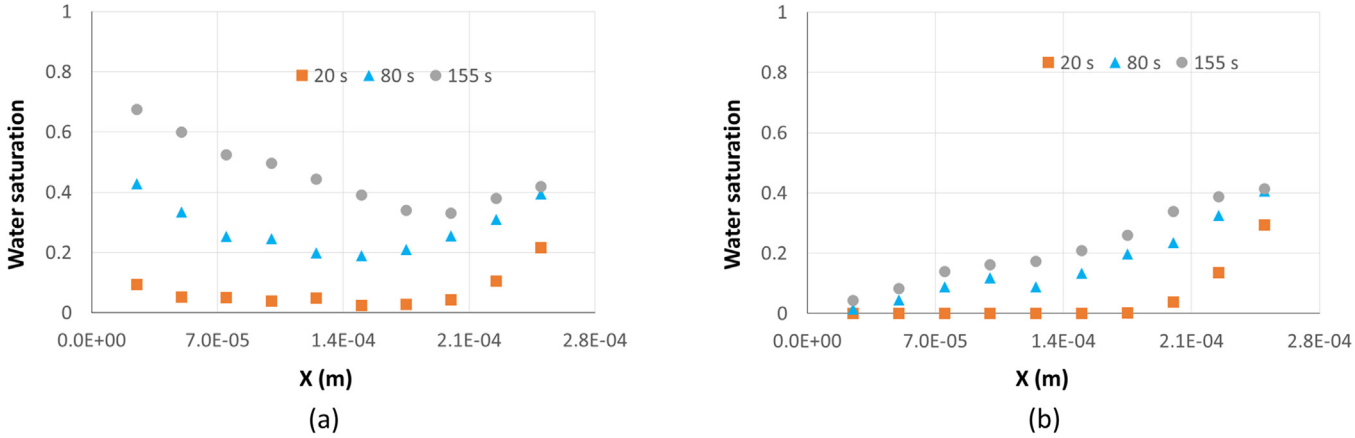

Fig. 15. Water saturation profiles along the through-plane direction at three time instances: (a) for the GDL with the high thermal conductivity, and (b) for the GDL with the low thermal conductivity.

rate under low capillary number values. This is in accordance with experimental observations (Deevanhxay et al., 2013; Lee et al., 2015), which was further confirmed by our PDMS micromodel-based drainage experiment (see Appendix A). Obviously, this cannot be predicted by the Darcy's law with conventionally measured material properties (Qin and Hassanizadeh, 2015), unless a capillary-number-dependent relative permeability is provided under low capillary number values.

For low capillary number flows in a thin porous layer under either pressure or flow rate boundary condition, our pore-network modeling predicted a concave profile of water saturation distribution along the layer thickness. However, a convex saturation profile was always predicted by the Darcy's law (Rebai and Prat, 2009) as explained in Section 4.1.

To sum up, the two-phase Darcy's law with conventionally measured material properties cannot be used to model extremely low capillary number flow through thin porous layers for two reasons: (1) the failure of the REV concept, and (2) the failure of the measurement of material properties under low capillary number values. Based on our pore-scale studies, it is confirmed that water migration in the layer under small capillary number values (e.g., the operation regime of PEFCs) is percolation-based; its distribution is mainly determined by the pore structures. When modeling at the REV scale, the dynamics of water migration may be considerably simplified. For instance, only the mass balance is needed to track the water distribution, together with upscaled geometric information.

From the test case 2, it is seen that the water distribution profile along the through-plane direction in the coarse layer was directly related to the breakthrough points at the layer interface. A non-monotonic water profile was seen when there were few breakthrough points at the layer interface. Meanwhile, much less water presented in the coarse layer. The similar phenomenon was also observed in the experiment of water flooding in PEFCs

(Lee et al., 2015). However, the authors only attributed the non-monotonic water profile to the heterogeneity of the GDL pores along the through-plane direction. When an MPL is used in the cathode of a PEFC, at a relatively low operating temperature (i.e., phase change is not dominant in the water removal), it can reduce water flooding in the GDL by limiting its access to liquid water at the MPL-GDL interface. In addition, the pore size of the MPL is comparable to that of the CL, such that the CL will not be fully covered by liquid water. That is why the MPL is required for water management at high current densities (Nam et al., 2009). From the nonmonotonic saturation profile, it is observed that at the average scale water migrated from low saturation to high saturation along the through-plane direction. This definitely cannot be predicted by the extended Darcy's law.

The GDL is the thickest porous layer in a PEFC, which may result in large mass activation loss (O'hayre and Cha, 2016). In the test case 3, by playing with the thermal conductivity of GDL, we showed the crucial role of phase change in reducing liquid water flooding in the GDL. By building up a relatively large thermal gradient along the layer thickness, water condensation can be localized just under the land area (see Fig. 14). Subsequently, liquid water migrated back to the MPL-GDL under the capillary action. With the GDL of high thermal conductivity, severe water flooding was found, which indicates that the addition of an MPL is necessary to mitigate water flooding in the GDL. However, with the GDL of low thermal conductivity, large thermal gradients can cause water to be removed mainly in the form of water vapor, which notably mitigates water flooding in the GDL. In this case, the addition of an MPL would have litter influence on the GDL performance. Our numerical findings are in consistence with the experimental observations by Owejan et al. (2010). When phase change is dominant in the GDL, to relieve water flooding, practically a coarser layer may be added between the BP and the conventional GDL. This would enhance liquid water removal towards the hydrophilic GC, and meanwhile prevent water migration back into the MPL-GDL.

6. Conclusions

A dynamic pore-network model, as an effective pore-scale model, has been developed to understand air-water flow thought thin porous layers, particularly under low capillary number values. One typical application is water management in low-temperature PEFCs. Three test cases were conducted to shed light on developing an efficient and reliable continuum-scale PEFC model, the utilization of a bilayer for regulating flow and transport, and the role of phase change in water flooding in the GDL. Specifically, we conclude the following:

(1) Under low capillary number values (in the regime of quasi-static), the extended Darcy's law with conventionally measured material properties is not applicable to water transport in a hydrophobic thin porous layer. Without phase change, water pathways in the layer is insensitive to the imposed flow rate. This indicates that at the REV scale the modeling of water flooding in the diffusion layers of a PEFC can be simplified dramatically.
(2) For a bilayer of fine and coarse thin porous layers, when water invades from the fine layer to the coarse layer, water pathways and distribution in the coarse layer are mainly determined by the breakthrough points at the layer-layer interface. This could explain why the MPL can reduce water flooding in the GDL. Furthermore, a nonmonotonic saturation profile may be built up along the coarse layer thickness.
(3) When phase change is dominant in the water removal, by reducing the thermal conductivity of GDL moderately, condensation of vapor can be localized just underneath the land area. Furthermore, to prevent liquid water invading back the MPL-GDL, a slightly coarser layer compared to the GDL may be added between the BP and the GDL. This would keep the pores under the land dry and enhance the reactant diffusion into the CL.

Acknowledgment

C.Z.Q. and M.C. acknowledge the support of Darcy Center of Utrecht University and Eindhoven University of Technology. R.W. acknowledges the support of National Natural Science Foundation of China (No. 51776122).

Declaration of interests

None declared.

Appendix A. PDMS micromodel-based drainage experiment under small capillary number values

With the help of micromodel experiments, we demonstrate that under extremely small capillary number values, liquid water distribution in the layer at the breakthrough is insensitive to the imposed flow rate. This is because they are very close to the quasi-static regime.

Fig. A1 shows the used PDMS micromodel. The porous domain is composed of ducts of the same length and depth but various widths. The length and depth are 1000 μm and 100 μm respectively. The width is varied from 50 μm to 500 μm. The number of ducts is 30 and 5 in the x and y directions, respectively. The top of the micromodel faces an outlet channel, while its bottom is connected to a water reservoir.

Initially, the micromodel was saturated with air. Then, liquid water as the nonwetting phase was injected into the domain using a syringe pump (Harvard Apparatus, 11 Plus, USA). The injection

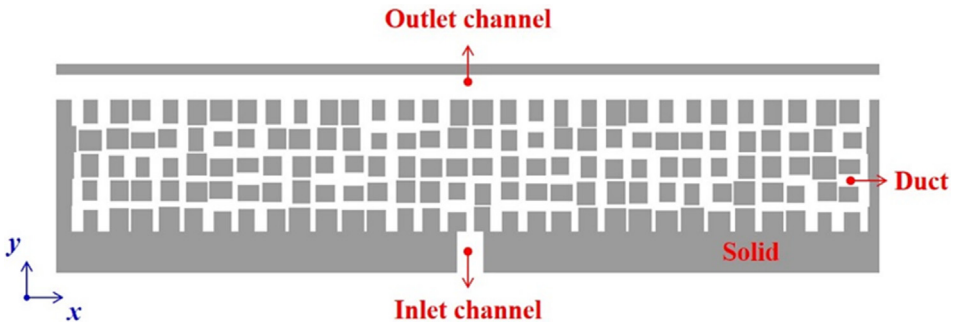

Fig. A1. Schematic of the used PDMS micromodel.

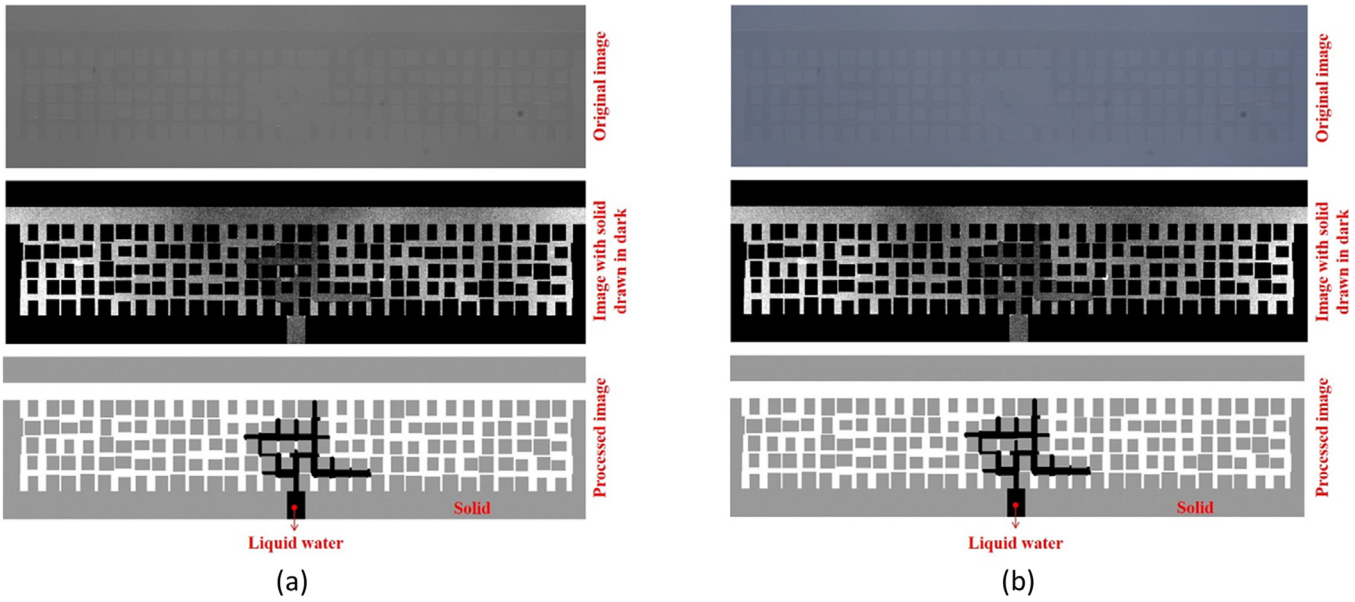

Fig. A2. Liquid water distribution patterns at the breakthrough moment under two different inject rates: (a) 1 μl/min, and (b) 10 μl/min. The two flow rates correspond to the capillary number values of 10^{-7} and 10^{-6}. In the calculation of capillary number, the velocity was computed by averaging the flow rate over the whole cross section of the micromodel.

was stopped, once liquid water reached the breakthrough. The process of water invasion was recorded using a high-speed camera (Vision Research, Phantom V5.1, USA) equipped with a macro lens (Tokina, 100F2.8D, Japan). In the experiment, dye agent was not used in liquid water to avoid alteration of the wettability. The obtained images need to be processed to present clearly the distributions of liquid water in the micromodel. The detailed image processing procedure can be found in Wu et al. (2016).

Two injection rates were used in the experiment, i.e. 1 μl/min and 10 μl/min, which correspond to the capillary number values of 10^{-7} and 10^{-6}, respectively. The distributions of liquid water at the breakthrough in the two cases were compared in Fig. A2. The final distributions were almost the same, except one more duct was invaded for the flow rate of 10 μl/min.

Appendix B. Supplementary material

Supplementary data to this article can be found online at https://doi.org/10.1016/j.ces.2019.03.038.

References

Basu, S., Wang, C.Y., Chen, K.S., 2009. Phase change in a polymer electrolyte fuel cell. J. Electrochem. Soc. 156, B748–B756. https://doi.org/10.1149/1.3115470.

Belgacem, N., Agaësse, T., Pauchet, J., Prat, M., 2016. Liquid invasion from multiple inlet sources and optimal gas access in a two-layer thin porous medium. Transp. Porous Media 115, 449–472. https://doi.org/10.1007/s11242-016-0630-1.

Berg, S., Ott, H., Klapp, S.a., Schwing, A., Neiteler, R., Brussee, N., Makurat, A., Leu, L., Enzmann, F., Schwarz, J.-O., Kersten, M., Irvine, S., Stampanoni, M., 2013. Real-time 3D imaging of Haines jumps in porous media flow. Proc. Natl. Acad. Sci. U. S. A. 110, 3755–3759. https://doi.org/10.1073/pnas.1221373110.

Blunt, M.J., Jackson, M.D., Piri, M., Valvatne, P.H., 2002. Detailed physics, predictive capabilities and macroscopic consequences for pore-network models of multiphase flow. Adv. Water Resour. 25, 1069–1089. https://doi.org/10.1016/S0309-1708(02)00049-0.

Deevanhxay, P., Sasabe, T., Tsushima, S., Hirai, S., 2013. Observation of dynamic liquid water transport in the microporous layer and gas diffusion layer of an operating PEM fuel cell by high-resolution soft X-ray radiography. J. Power Sources 230, 38–43. https://doi.org/10.1016/j.jpowsour.2012.11.140.

Diersch, H.J.G., Clausnitzer, V., Myrnyy, V., Rosati, R., Schmidt, M., Beruda, H., Ehrnsperger, B.J., Virgilio, R., 2011. Modeling unsaturated flow in absorbent swelling porous media: Part 2. Numerical simulation. Transp. Porous Media 86, 753–776. https://doi.org/10.1007/s11242-010-9650-4.

Fazeli, M., Hinebaugh, J., Bazylak, A., 2015. Investigating inlet condition effects on PEMFC GDL liquid water transport through pore network modeling. J. Electrochem. Soc. 162, F661–F668. https://doi.org/10.1149/2.0191507jes.

García-Salaberri, P.a., Hwang, G., Vera, M., Weber, A.Z., Gostick, J.T., 2015. Effective diffusivity in partially-saturated carbon-fiber gas diffusion layers: Effect of through-plane saturation distribution. Int. J. Heat Mass Transf. 86, 319–333. https://doi.org/10.1016/j.ijheatmasstransfer.2015.02.073.

Pinder, George F., Gray, 2008. Essentials of Multiphase Flow and Transport in Porous Media. John Wiley & Sons Inc..

Gostick, J.T., Ioannidis, M.A., Fowler, M.W., Pritzker, M.D., 2007. Pore network modeling of fibrous gas diffusion layers for polymer electrolyte membrane fuel cells. J. Power Sources 173, 277–290. https://doi.org/10.1016/j.jpowsour.2007.04.059.

Hassanizadeh, S.M., Gray, W.G., 1990. Mechanics and thermodynamics of multiphase flow in porous media including interphase boundaries. Adv. Water Resour. 13, 169–186. https://doi.org/10.1016/0309-1708(90)90040-B.

Huang, X., Bandilla, K.W., Celia, M.A., 2016. Multi-physics pore-network modeling of two-phase shale matrix flows. Transp. Porous Media 111, 123–141. https://doi.org/10.1007/s11242-015-0584-8.

Ji, Y., Luo, G., Wang, C.-Y., 2010. Pore-level liquid water transport through composite diffusion media of PEMFC. J. Electrochem. Soc. 157, B1753. https://doi.org/10.1149/1.3491359.

Joekar-Niasar, V., Hassanizadeh, S.M., Dahle, H.K., 2010. Non-equilibrium effects in capillarity and interfacial area in two-phase flow: dynamic pore-network modelling. J. Fluid Mech. 655, 38–71. https://doi.org/10.1017/S0022112010000704.

Kunz, P., Zarikos, I.M., Karadimitriou, N.K., Huber, M., Nieken, U., Hassanizadeh, S.M., 2016. Study of multi-phase flow in porous media: comparison of SPH simulations with micro-model experiments. Transp. Porous Media 114, 581–600. https://doi.org/10.1007/s11242-015-0599-1.

Lee, J., Yip, R., Antonacci, P., Ge, N., Kotaka, T., Tabuchi, Y., Bazylak, A., 2015. Synchrotron investigation of microporous layer thickness on liquid water distribution in a PEM fuel cell. J. Electrochem. Soc. 162, F669–F676. https://doi.org/10.1149/2.0221507jes.

Lee, K.-J., Nam, J.H., Kim, C.-J., 2009. Pore-network analysis of two-phase water transport in gas diffusion layers of polymer electrolyte membrane fuel cells. Electrochim. Acta. https://doi.org/10.1016/j.electacta.2008.08.068.

Ma, S., Mason, G., Morrow, N.R., 1996. Effect of contact angle on drainage and imbibition in regular polygonal tubes. Colloids Surf. A Physicochem. Eng. Asp. 117, 273–291. https://doi.org/10.1016/0927-7757(96)03702-8.

Médici, E.F., Allen, J.S., 2013. Evaporation, two phase flow, and thermal transport in porous media with application to low-temperature fuel cells. Int. J. Heat Mass Transf. 65, 779–788. https://doi.org/10.1016/j.ijheatmasstransfer.2013.06.035.

Morgan, J.M., Datta, R., 2014. Understanding the gas diffusion layer in proton exchange membrane fuel cells. I. How its structural characteristics affect diffusion and performance. J. Power Sources 251, 269–278. https://doi.org/10.1016/j.jpowsour.2013.09.090.

Mukherjee, P.P., Wang, C.Y., Kang, Q., 2009. Mesoscopic modeling of two-phase behavior and flooding phenomena in polymer electrolyte fuel cells. Electrochim. Acta 54, 6861–6875. https://doi.org/10.1016/j.electacta.2009.06.066.

Nam, J.H., Lee, K.J., Hwang, G.S., Kim, C.J., Kaviany, M., 2009. Microporous layer for water morphology control in PEMFC. Int. J. Heat Mass Transf. 52, 2779–2791. https://doi.org/10.1016/j.ijheatmasstransfer.2009.01.002.

Owejan, J.P., Owejan, J.E., Gu, W., Trabold, T.a., Tighe, T.W., Mathias, M.F., 2010. Water transport mechanisms in PEMFC gas diffusion layers. J. Electrochem. Soc. 157, B1456. https://doi.org/10.1149/1.3468615.

Park, J., Oh, H., Ha, T., Il, Y., Min, K., 2015. A review of the gas diffusion layer in proton exchange membrane fuel cells: Durability and degradation. Appl. Energy 155, 866–880. https://doi.org/10.1016/j.apenergy.2015.06.068.

Patzek, T.W., 2001. Verification of a complete pore network simulator of drainage and imbibition. SPE J. 6, 144–156. https://doi.org/10.2118/71310-PA.

Prat, M., Agaësse, T., 2015. Thin porous media. In: Vafai, Kambiz (Ed.), Handbook of Porous Media. CRC Press.

Qin, C.-Z., Hassanizadeh, S., Van Oosterhout, L., 2016. Pore-network modeling of water and vapor transport in the micro porous layer and gas diffusion layer of a polymer electrolyte fuel cell. Computation 4, 21. https://doi.org/10.3390/computation4020021.

Qin, C., 2015. Water transport in the gas diffusion layer of a polymer electrolyte fuel cell: dynamic pore-network modeling. J. Electrochem. Soc. 162, F1036–F1046. https://doi.org/10.1149/2.0861509jes.

Qin, C., Hassanizadeh, S.M., Rensink, D., Fell, S., 2012a. One-dimensional phenomenological model for liquid water flooding in cathode gas channel of a polymer electrolyte fuel cell. J. Electrochem. Soc. 159, B737. https://doi.org/10.1149/2.092206jes.

Qin, C., Rensink, D., Fell, S., Majid Hassanizadeh, S., 2012b. Two-phase flow modeling for the cathode side of a polymer electrolyte fuel cell. J. Power Sources 197, 136–144. https://doi.org/10.1016/j.jpowsour.2011.08.095.

Qin, C., Rensink, D., Hassanizadeh, S., 2012c. Direct simulation of liquid water dynamics in the gas channel of a polymer electrolyte fuel cell. J. Electrochem. Soc. 159, 434–443. https://doi.org/10.1149/2.004205jes.

Qin, C.Z., Hassanizadeh, S.M., 2015. A new approach to modelling water flooding in a polymer electrolyte fuel cell. Int. J. Hydrogen Energy 40, 3348–3358. https://doi.org/10.1016/j.ijhydene.2015.01.035.

Qin, C.Z., Hassanizadeh, S.M., 2014. Multiphase flow through multilayers of thin porous media: General balance equations and constitutive relationships for a solid-gas-liquid three-phase system. Int. J. Heat Mass Transf. 70, 693–708. https://doi.org/10.1016/j.ijheatmasstransfer.2013.11.059.

Raeini, A.Q., Blunt, M.J., Bijeljic, B., 2014. Direct simulations of two-phase flow on micro-CT images of porous media and upscaling of pore-scale forces. Adv. Water Resour. 74, 116–126. https://doi.org/10.1016/j.advwatres.2014.08.012.

Ransohoff, T.C., Engineering, C., 1988. Laminar flow of a wetting liquid along the corners of a predominantly gas-occupied noncircular pore 12, 392–401.

Rebai, M., Prat, M., 2009. Scale effect and two-phase flow in a thin hydrophobic porous layer. Application to water transport in gas diffusion layers of proton exchange membrane fuel cells. J. Power Sources 192, 534–543. https://doi.org/10.1016/j.jpowsour.2009.02.090.

Riasi, M.S., Palakurthi, N.K., Montemagno, C., Yeghiazarian, L., 2016. A feasibility study of the pore topology method (PTM), a medial surface-based approach to multi-phase flow simulation in porous media. Transp. Porous Media 115, 519–539. https://doi.org/10.1007/s11242-016-0720-0.

Ryan O'hayre, W.G.C., Cha, Suk-Won, 2016. Fuel cell fundamentals. Wiley. https://doi.org/10.1017/CBO9781107415324.004.

Sadeghifar, H., Djilali, N., Bahrami, M., 2014. Effect of Polytetrafluoroethylene (PTFE) and micro porous layer (MPL) on thermal conductivity of fuel cell gas diffusion layers: Modeling and experiments. J. Power Sources 248, 632–641. https://doi.org/10.1016/j.jpowsour.2013.09.136.

Shokrpour Roudbari, M., van Brummelen, E.H., Verhoosel, C.V., 2016. A multiscale diffuse-interface model for two-phase flow in porous media. Comput. Fluids 141, 212–222. https://doi.org/10.1016/j.compfluid.2016.07.006.

Sinha, P.K., Mukherjee, P.P., Wang, C.-Y., 2007. Impact of GDL structure and wettability on water management in polymer electrolyte fuel cells. J. Mater. Chem. https://doi.org/10.1039/b703485g.

Sinha, P.K., Wang, C.-Y., 2007. Pore-network modeling of liquid water transport in gas diffusion layer of a polymer electrolyte fuel cell. Electrochim. Acta 52, 7936–7945. https://doi.org/10.1016/j.electacta.2007.06.061.

Straubhaar, B., Pauchet, J., Prat, M., 2016. Pore network modelling of condensation in gas diffusion layers of proton exchange membrane fuel cells. Int. J. Heat Mass Transf. 102, 891–901. https://doi.org/10.1016/j.ijheatmasstransfer.2016.06.078.

Sweijen, T., Nikooee, E., Hassanizadeh, S.M., Chareyre, B., 2016. The effects of swelling and porosity change on capillarity: DEM coupled with a pore-unit assembly method. Transp. Porous Media 113, 207–226. https://doi.org/10.1007/s11242-016-0689-8.

Tavangarrad, A.H., Mohebbi, B., Hassanizadeh, S.M., Rosati, R., Claussen, J., Blümich, B., 2018. Continuum-scale modeling of liquid redistribution in a stack of thin hydrophilic fibrous layers. Transp Porous Media. https://doi.org/10.1007/s11242-018-0999-0.

Thompson, K.E., 2002. Pore-scale modeling of fluid transport in disordered fibrous materials. AIChE J. 48, 1369–1389. https://doi.org/10.1002/aic.690480703.

Valvatne, P.H., Blunt, M.J., 2004. Predictive pore-scale modeling of two-phase flow in mixed wet media. Water Resour. Res. 40, 1–21. https://doi.org/10.1029/2003WR002627.

Wang, Y., Wang, C., 2008. A nonisothermal, two-phase model for polymer electrolyte. Fuel Cells. https://doi.org/10.1149/1.2193403.

Wang, Z., Yang, J., Koo, B., Stern, F., 2009. A coupled level set and volume-of-fluid method for sharp interface simulation of plunging breaking waves. Int. J. Multiph. Flow 35, 227–246. https://doi.org/10.1016/j.ijmultiphaseflow.2008.11.004.

Wargo, E.A., Schulz, V.P., Cecen, A., Kalidindi, S.R., Kumbur, E.C., 2013. Resolving macro- and micro-porous layer interaction in polymer electrolyte fuel cells using focused ion beam and X-ray computed tomography. Electrochim. Acta 87, 201–212. https://doi.org/10.1016/j.electacta.2012.09.008.

Wu, R., Kharaghani, A., Tsotsas, E., 2016. Capillary valve effect during slow drying of porous media. Int. J. Heat Mass Transf. 94, 81–86. https://doi.org/10.1016/j.ijheatmasstransfer.2015.11.004.

Wu, R., Liao, Q., Zhu, X., Wang, H., 2012a. Impacts of the mixed wettability on liquid water and reactant gas transport through the gas diffusion layer of proton exchange membrane fuel cells. Int. J. Heat Mass Transf. 55, 2581–2589. https://doi.org/10.1016/j.ijheatmasstransfer.2012.01.002.

Wu, R., Liao, Q., Zhu, X., Wang, H., 2012b. Liquid and oxygen transport through bilayer gas diffusion materials of proton exchange membrane fuel cells. Int. J. Heat Mass Transf. 55, 6363–6373. https://doi.org/10.1016/j.ijheatmasstransfer.2012.06.019.

Yang, J., Bondino, I., Regaieg, M., Moncorgé, A., 2017. Pore to pore validation of pore network modelling against micromodel experiment results. Comput. Geosci. 21, 849–862. https://doi.org/10.1007/s10596-017-9630-7.

Zhuang, L., Hassanizadeh, S.M., Qin, C., Waal, A. De, 2017. Experimental investigation of hysteretic dynamic capillarity effect in unsaturated flow. https://doi.org/10.1002/2017WR020895.